Alexandria Engineering Journal (2023) 70, 685–699

Alexandria University

Alexandria Engineering Journal

www.elsevier.com/locate/aej
www.sciencedirect.com

ORIGINAL ARTICLE

Computational fluid dynamics prediction of the aerodynamic difference between stationary and moving trains

Bin Xu [a,b,c], Tanghong Liu [a,b,c], Yutao Xia [a,b,c], Wenhui Li [a,b,c], Xiaoshuai Huo [a,b,c], Hongrui Gao [a,b,c], Zhengwei Chen [d], Hongkang Liu [a,b,c,*]

[a] *Key Laboratory of Traffic Safety on Track of Ministry of Education, School of Traffic & Transportation Engineering, Central South University, Changsha 410075, China*
[b] *Joint International Research Laboratory of Key Technology for Rail Traffic Safety, Central South University, Changsha 410075, Hunan, China*
[c] *National & Local Joint Engineering Research Center of Safety Technology for Rail Vehicle, Changsha 410075, China*
[d] *Department of Civil and Environmental Engineering, The Hong Kong Polytechnic University, Hung Hom, Kowloon, Hong Kong Special Administrative Region*

Received 15 September 2022; revised 7 February 2023; accepted 8 March 2023
Available online 20 March 2023

KEYWORDS

CFD;
Moving train;
Aerodynamic characteristics;
Vortex;
Slipstream

Abstract Moving model simulations have been a key method of predicting the aerodynamic performances of High-Speed Trains (HSTs). Ideally, the aerodynamic characteristics of a train moving or being blown by the wind are the same with appropriate ground configurations. In a numerical simulation, there are differences due to interpolation errors and errors caused by model movement. The impact of the error caused by the movement on the result is not known. Therefore, in this study, stationary and moving cases were used to assess the magnitude of the movement's effect using the Improved Detached Eddy Simulation (IDDES) method. A wind tunnel test validated the numerical algorithm at 60 m/s and a common yaw angle of 0°. Moreover, the spatial and time discretization satisfied the high accuracy requirements, as determined through a mesh independence study and convective Courant number testing. The time-averaged drag coefficients predicted by the moving case were similar to those of the stationary case, especially the total drag coefficients. In contrast, differences were determined in the stationary and moving cases in terms of the flow structure and slipstream. The motion encouraged the streamwise vortices around the tail car and the wake vortices to expand along the spanwise direction and the wall-normal direction, and the vortex cores shifted away from the outer surface of the vehicle. As a consequence, the average value and the standard deviation of the slipstream increased. Therefore, moving model simulations require

* Corresponding author at: Key Laboratory of Traffic Safety on Track of Ministry of Education, School of Traffic & Transportation Engineering, Central South University, Changsha 410075, China.
E-mail address: liuhongkang@csu.edu.cn (H. Liu).

Peer review under responsibility of Faculty of Engineering, Alexandria University.

https://doi.org/10.1016/j.aej.2023.03.022

more caution. These findings can help researchers make directional corrections in the numerical simulation of train-tunnel systems.

1. Introduction

The aerodynamic performances of high-speed trains have long been a focus of research. In research on the aerodynamic performances of high-speed trains, there are four main methods: full-scale testing, model-scale testing, Computational Fluid Dynamics (CFD), and analytical methods [1]. The data obtained from full-scale tests are discrete, and these tests are costly and difficult to perform [2]. The boundary layer in a wind tunnel test is a detrimental problem that directly interferes with the accuracy of the measurement results of the slipstream and drag [3–5]. Although a moving model test can restore the relative motion between a vehicle and the ground, it is difficult to attain high-resolution and satisfactory results due to the complexity of these tests [6]. CFD has become an important research method in the pre-research stage because it can decompose the flow into much smaller turbulence scales, which are much smaller than those measured in experiments [7].

In most studies, the results of the model tests and numerical simulations are consistent whether a train is running on a track [8] or in a crosswind [9–11], so long as moving wall boundary conditions are used on the ground [4,5]. However, the relative wind velocity, which is commonly used to simulate the operation of high-speed trains in crosswinds, does not correctly deal with the relative movement between the infrastructure and a High-Speed Train (HST). Several researchers [12–14] have found that although the aerodynamic forces on HSTs are slightly affected by the relative movement, the velocity field is strongly affected. When predicting the aerodynamic forces of trains passing through bridges and tunnels or passing by each other [15], a moving simulation must be adopted to correctly replicate the relative motion; in summary, mesh movement is necessary in many cases.

The use of an overset mesh is a technique introduced by Simcenter STAR-CCM + for dealing with multiple or moving bodies. This technique has been widely tested by scholars [16–19]. However, there is little research on the reliability of an overset mesh applied to trains. Ideally, the aerodynamic characteristics of a train blown by the wind on moving ground and those of a train moving on stationary ground are the same. However, there may be differences between the two cases due to the mesh movement. The accuracy of the conclusion cannot be controlled while analyzing the stationary case and the moving case.

Errors can be divided into two types: mesh interpolation errors and errors caused by mesh movement. It is well known that the coupling of an overset mesh and a background mesh introduces interpolation errors, which have the same order of magnitude as other discretization errors [20]. Therefore, interpolation errors can be ignored if the mesh is reasonable. However, at present, it is unknown what effect mesh movement will have on the result. Research on the overset mesh for HSTs in motion is lacking. Thus, in this research, two calculation cases are examined, namely, a stationary case and a moving case, to study the influence of the motion of an overset mesh on the aerodynamic force and flow field structures of HSTs. This will help researchers understand the error generated by the model movement. Furthermore, an appropriate directional correction is made to the results of numerical simulations that include the train passing through a tunnel or a windbreak wall.

The structure of this paper is as follows. In the second section, the model, calculation domain, boundary conditions, meshing strategy, and numerical methods are described. In the third section, the mesh independence and numerical method study is presented. In the fourth section, the results are analyzed. In the fifth section, conclusions are provided.

2. Numerical method

2.1. Geometric model

The geometric model was a 1/8 model of the CRH2, which had available experimental data [21] and was convenient for validation. The model included a head car, a middle car, and a tail car. The pantograph was ignored, and the basic contour characteristics of the side and roof of the train were modeled well, as shown in Fig. 1. It should be noted that to clearly show the details, the model scales were not the same. There was a 64-mm gap between the windshields at the full scale [22], which was consistent with the wind tunnel test settings. The windshield included an outer windshield and an inner windshield, which could truly reflect the separation of the fluid at that position. The full-scale bogies retained larger structural features that were more than 100 mm in size [23]. The full-scale train wheels were reduced by 40 mm to avoid contact with the track and keep the ground clearance unchanged in the numerical validation[23,24]. The full-scale train had a height of 3.7 m, a width of 3.4 m, a length of 25.7 m for the head and tail cars, and a length of 25.0 m for the middle car. The characteristic height was defined as $H = \frac{3.7}{8} = 0.4625$ m.

2.2. Computational domain and boundary conditions

For both the stationary and moving cases, an overset mesh was used to ensure that the same interpolation error occurred in the coupled regions. The calculation domain was divided into two parts. The background region contained the entire solution domain and the overset region contained the moving objects and their surroundings. The sizes of the two regions are shown in Fig. 2. The background region had a height of $10H$ and a width of 20H. The size of the background region was sufficient for the full development of the flow field [25]. There was no correction to the simulation results because the blocking ratio was 0.016, which was less than 0.05 [26]. In the stationary case, as shown in Table 1, the upstream size A of the background region was $10H$, while the downstream size B was 30H [25]. In the moving case, the upstream size A of the

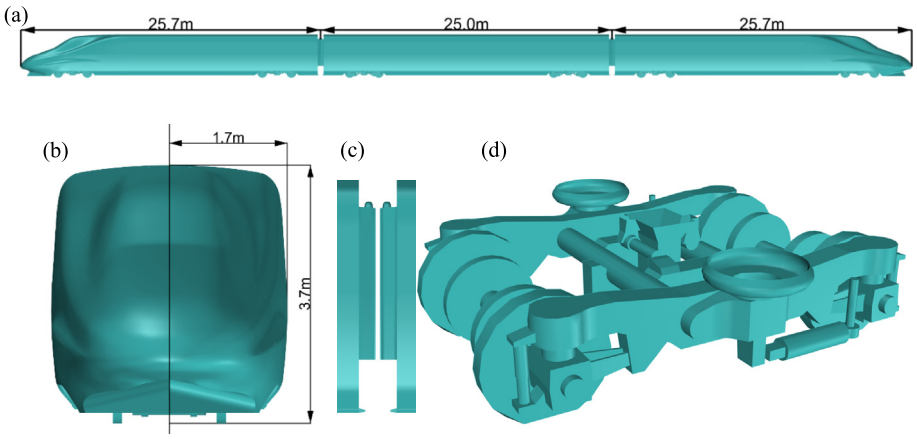

Fig. 1 CRH2 model: (a) side view, (b) front view, (c) windshield, and (d) bogie.

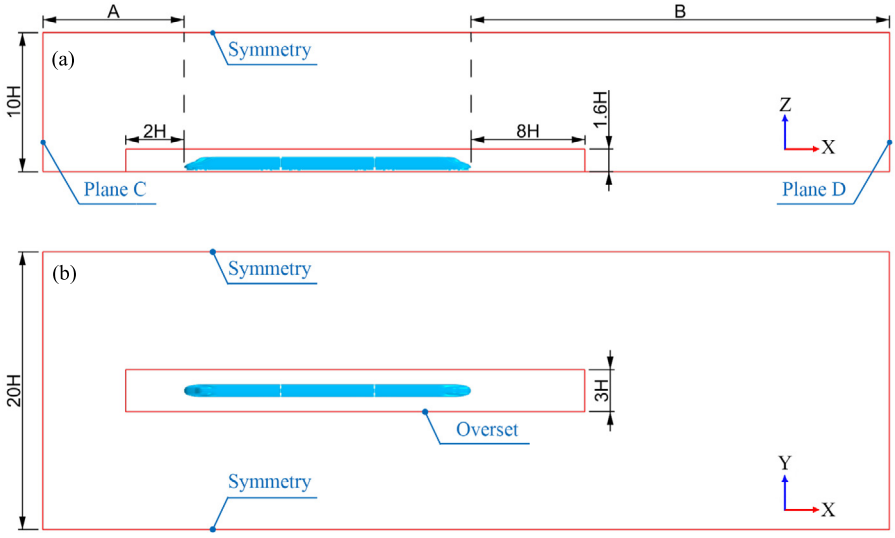

Fig. 2 Schematic diagram of the computational domain: (a) side view and (b) top view.

Table 1 Setting of boundary conditions.

Case	A	B	Plane C	Plane D	Ground
Stationary case	10H	30H	Velocity inlet	Pressure outlet	No-slip moving wall
Moving case	86H	16H	Pressure outlet	Stagnation inlet	No-slip stationary wall

background region was 86H, which was sufficient for the train to move 0.6 s in the negative X-direction at a speed of 60 m/s and to ensure that the distance from the overset mesh to Plane C was 4H when the motion was over. The downstream size B was 16H [26]. The height of the overset region was 1.6H and the width was 3H. The upstream length of CRH2 in the overset region was 2H and the downstream length was 8H. Two symmetric and opposite streamwise vortices were generated at the end of the tail car [27,28]. These vortices were of interest for this analysis. The streamwise vortices expanded along the spanwise direction [29], so the width of the overset in the wake area had to be slightly larger than the width of the vehicle to avoid high-pressure gradients at the overset mesh boundaries and reduce interpolation errors. This was also the reason for setting the 2H and 8H dimensions.

In the two cases, both the sides and the top of the background boundaries were set to the symmetry plane [16]. In the stationary case, Plane C was defined as the velocity inlet with a turbulence intensity of 1% and velocity of 60 m/s, which simulated the low-turbulence horizontal free flow in the wind tunnel [30]. Plane D was defined as a pressure outlet, and the tangential speed of the ground was set to 60 m/s in the X-direction. In the moving case, the overset region moved in the X-direction at a speed of − 60 m/s. Plane C was defined

as a pressure outlet. Plane D was defined as a stagnation inlet [16], and the ground was a no-slip stationary wall.

2.3. Meshing strategy

The mesh was generated by a STAR-CCM + trimmed mesher, which was suitable for the numerical simulation of the external flow field. The mesh of the surroundings and the wake of the vehicle was refined to capture the subtle changes in the flow field and became sparser as it deviated from the vehicle, as shown in Fig. 3. The overset mesh was colored red, and the blue mesh was generated from the background region. Both meshes were coupled at their interface. The prism layers, which allowed the solver to resolve the near-wall flow accurately, were generated next to the wall surface. To verify the adequacy of the mesh resolution while using the same refinement boxes, the train surfaces x + and z + and the size of the volume mesh were changed, excluding y+, where ×, y, and z denote the streamwise, wall-normal, and spanwise directions, respectively [31]. In the stationary case, three types of meshes were generated: coarse, medium, and fine meshes. The related parameters for the meshes are shown in Table 2. There were 16 prism layers near the train surface and six layers near the ground. Their growth rate was 1.2. The maximum of the train wall y + was less than 20, and the average value was less than 10.

2.4. Numerical model

The Large Eddy Simulation (LES) method can more accurately resolve the momentum, heat, and mass transfer in free shear flow at high Reynolds numbers than the Reynolds-

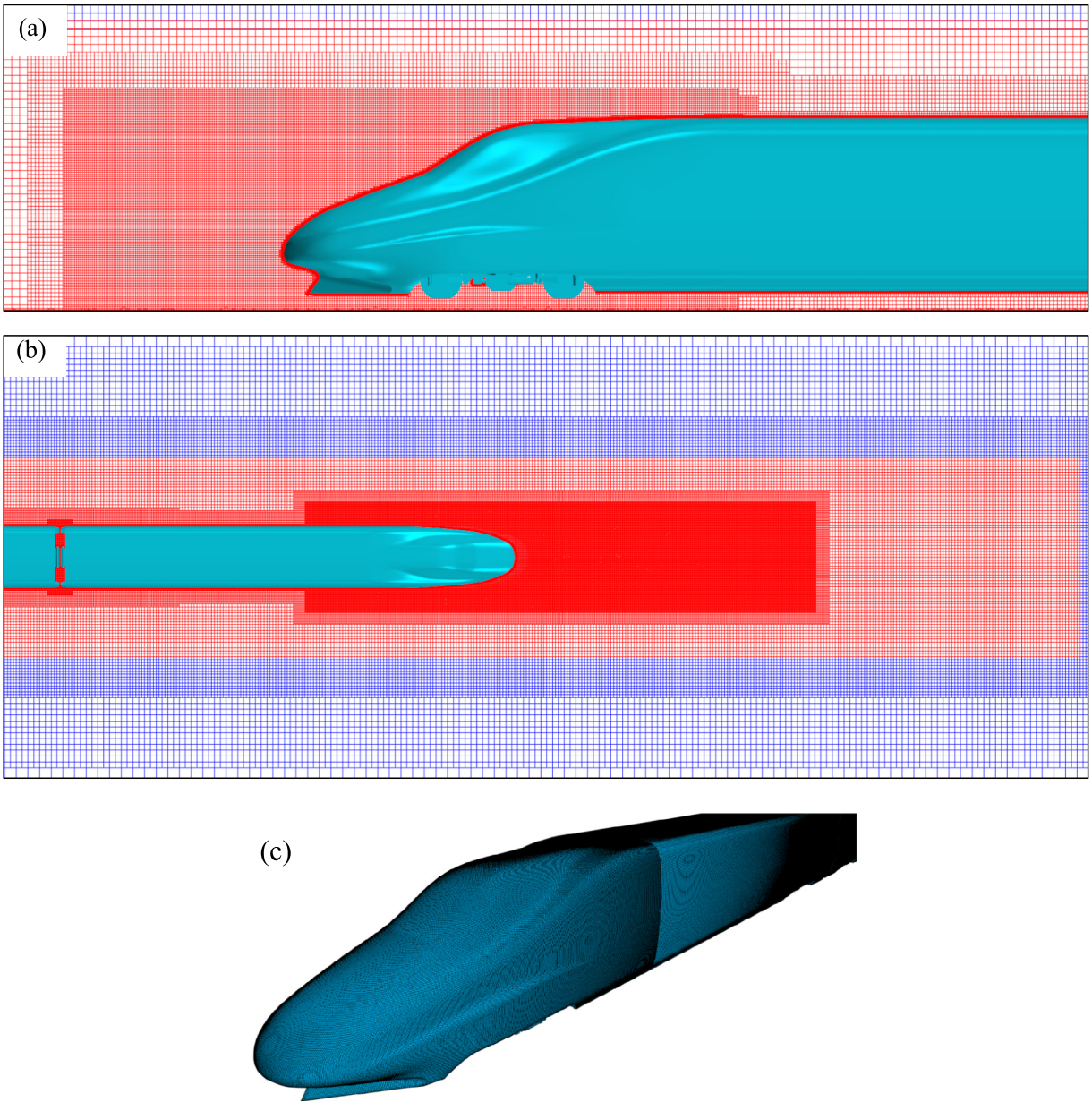

Fig. 3 Mesh around the high-speed train (HST): (a) front view of the upstream region, (b) top view of wake region, and (c) train surface mesh.

Table 2 Setting of mesh parameters.

Grids	x+	z+	Total numbers
Stationary coarse	500	500	35.8 million
Stationary medium	450	450	47.4 million
Stationary fine	400	400	64.8 million
Moving medium	450	450	57.6 million

averaged Navier-Stokes (RANS) method, and it can resolve a cascade of energy at large scales [32]. The cost of the LES method is an extremely high mesh accuracy with a huge number of calculations, which is unacceptable. In addition, the flow in the turbulent boundary layer does not have large eddies, which allows the use of the wall model to resolve the near-wall region to obtain the correct wall shear stress. Therefore, as a hybrid LES-RANS model, the Detached Eddy Simulation (DES) method uses the RANS method to resolve the boundary layers and the LES method to resolve the separated regions. The DES method has received attention and is widely used by scholars [30,33,34] because of its acceptable calculation cost and the resolution of large-scale separation vortices. In the Improved Delayed Detached Eddy Simulation (IDDES) method, premature separation, which is caused by ambiguous grid densities in thick boundary layers and shallow separation regions, and Log-Layer Mismatch (LLM) have been solved by [35] and [36], respectively. The IDDES method has excellent performance and was used in this study.

The segregated flow solver in STAR-CCM+, which uses the SIMPLE algorithm to deal with the pressure–velocity coupling, is appropriate for incompressible fluids with Mach numbers below 0.3 [20]. This approach has the advantage of speed and simplicity compared with the coupled flow solver.

The fluid in this study was assumed to be 15 °C air, with a density of 1.225 kg/m^3 and a dynamic viscosity of 1.78×10^{-5} Ns/m^2 [23]. The Reynolds number of the 1/8-scale HST was $Re = \frac{\rho u_\infty H}{\mu} = 1.9 \times 10^6$, meeting the requirement of being greater than 2.5×10^5 [26], where $u_\infty = 60$ m/s.

To accurately repeat the development of the wake vortex structure in each cycle, the time discretization format was second-order, the time step was $\Delta t \approx 0.005 T_{ref}$, and the number of inner iterations was eight, where $T_{ref} = \frac{H}{u_\infty}$. The convective Courant number is an important reference for determining the time step, which represents the number of grid elements that the fluid crosses per time step. Fig. 4 shows the convective Courant number of the moving case. The Courant number in the improved mesh region was mostly under 0.5, which met the requirement for high-precision predictions that the Courant number be less than 1. Large values exceeding 1 appeared only in the prism layer of the vehicle, and the proportion of such grid elements to the total was no more than 0.1%, which was acceptable [33,37].

Before performing simulations with the IDDES method (Shear Stress Transport (SST) $k-\omega$), the unsteady Reynolds-Averaged Navier-Stokes (URANS) method (SST $k-\omega$) was used to initialize the flow field to enhance the computational stability and accelerate convergence. The total calculation time was $T = 77.8 T_{ref}$, of which the URANS calculation time was $T_{URANS} = 6.5 T_{ref}$, and the IDDES calculation time was $T_{IDDES} = 71.3 T_{ref}$, which corresponded to a physical time of 4.8 s in the full-scale model. Fig. 5 shows the time history curve of the drag coefficients of the head car in the calculation process of the moving case. The formula for the drag coefficient is $C_d = \frac{F_d}{(0.5\rho u_\infty 2S)}$, where $S = 0.175$ m^2 is the cross-sectional area of the 1/8 HST and F_d represents the aerodynamic drag. The calculation results of the URANS showed high-frequency oscillations, but the drag coefficient C_d quickly converged. This helped the convergence of the IDDES calculations and stabilized the flow field development over a short period, which is displayed in the green region in the figure. Thus, it was appropriate to sample in the green region.

2.5. Numerical validation

This section compares the numerical calculation data with the wind tunnel test data and describes the verification of the independence of the mesh density to guarantee that the calculation was reliable. The CRH2 wind tunnel test results [22] have been adopted for numerous validations [14,38] because they are exceedingly reliable. It is important to select identical models to obtain consistent results for numerical simulations and wind tunnel tests. In the validation calculation, the track was added, which did not exist in our subsequent research and would have had a greater impact on the drag of the vehicle by changing the ground clearance and relative position. In addition, the calculation domain boundaries (except for the inlet and outlet) were set as no-slip stationary walls. Table 3 shows the drag coefficients of each vehicle in the numerical simulation and the wind tunnel test. The error of the head car was 3.4%, and the error of the tail car was 3.1%. Thus, the errors were both less than 5%, which was suitable for this study [38].

Table 4 shows the drag coefficients for the three grids. It should be noted that the mesh independence validation model did not include tracks. The C_d difference between the coarse grid and the fine grid was relatively large. The medium grid achieved high calculation accuracy with a reasonable number of grid elements, and the variation in the C_d of the head car between the medium grid and the fine grid did not exceed 1.5%.

Fig. 6 shows the time-averaged pressure coefficients along the centerline of the HST with the three grids. The pressure coefficient formula is $C_p = \frac{P-P_0}{(0.5\rho u_\infty^2)}$, where P is the pressure and P_0 is the reference static pressure. Although there were small discrepancies near the windshield and the nose of the tail car, this was caused by the violent flow separation, which was difficult to accurately simulate. Other positions on the surface of the HST showed high similarity, including the head car upstream. This indicated that the medium grid was suitable.

Fig. 7 shows the time-averaged streamwise velocity of the tail car. Compared with the time-averaged pressure coefficient, there was a modest deviation between the coarse grid and the fine grid, with the exception of the thickness of the boundary layer. The turning points of the asymptotic curves of the three grids were parallel. The velocity curve of the medium grid was in suitable agreement with the fine grid, so the medium grid was selected to maintain the calculation precision and reduce the calculation cost.

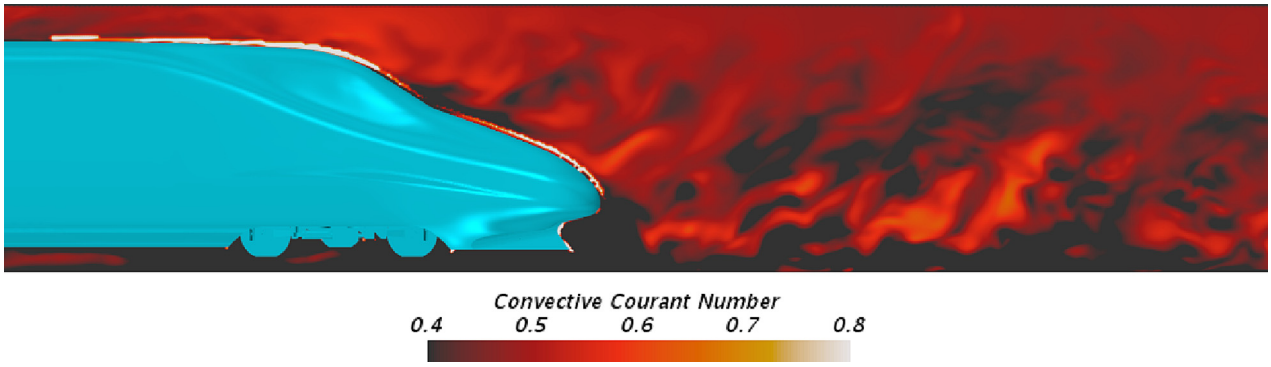

Fig. 4 Convective Courant number of the near-wake region in the moving case.

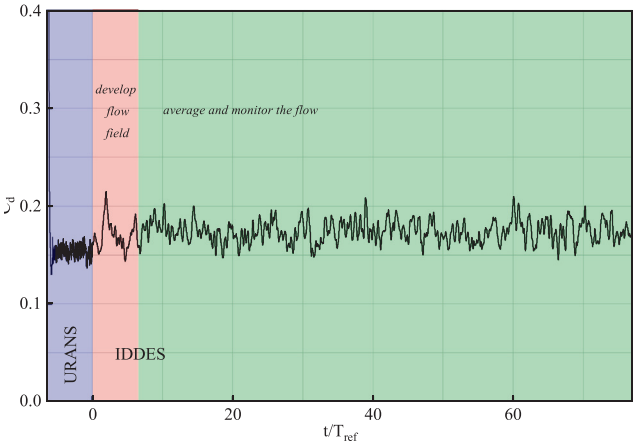

Fig. 5 Drag coefficient time history curve of the head car.

Table 3 Drag coefficients of the numerical simulation and wind tunnel test.

Cases	Drag coefficients		
	Head car	Middle car	Tail car
Wind tunnel test [22]	0.145	–	0.163
Numerical simulation (URANS)	0.143	0.081	0.158
Numerical simulation (IDDES)	0.150	0.085	0.158

Table 4 Drag coefficients from different grids.

Grids	Drag coefficients		
	Head car	Middle car	Tail car
Coarse	0.189	0.091	0.147
Middle	0.181	0.093	0.152
Fine	0.183	0.093	0.150

3. Results and analysis

3.1. Calculation efficiency

These calculations were performed at the High Performance Computing Platform of Central South University. The CPU used was an Intel(R) Xeon(R) Gold 6248R. Twenty CPUs were used in the stationary and moving cases, and each CPU had 48 cores. The calculation costs for the stationary and moving cases, excluding the URANS initialization times, were 55,104 and 63,360 core hours, respectively. Compared with the stationary case, the moving case had a higher calculation cost of approximately 15%. The grids in the overset region of the stationary and moving cases were the same, so the reason for the difference in the calculation costs was that the background region of the moving case was larger, resulting in a larger number of grid elements of more than 10.2 million. In addition, the overset region and the background region of the stationary case did not need to be recoupled at each time step.

The longer the physical time was, the larger the background region was in the moving case. This led to a significant increase in the number of grid elements and time steps. Furthermore, the inclusion of the mesh coupling required additional calculations. Thus, as the physical time increased, the calculation cost of the moving case far exceeded that of the stationary case.

3.2. Aerodynamic analysis

Table 5 shows the difference in the time-averaged C_d, including the viscous C_d and pressure C_d, where $C_d = \frac{F_d}{(0.5\rho u_\infty^2 S)}$ is the drag coefficient. The difference in the total C_d between the stationary and moving cases was only approximately 0.5%. The viscous drag coefficients of the moving case were always larger; those of the head car, middle car, and tail car for the moving case were 1.7%, 4.3%, and 4.4% larger, respectively. It was expected that the motion of the overset mesh would increase the wall shear stress slightly. The growth was only approximately 4%–4.5%, with the exception of the head car because the boundary layer emerged. The subsequent research focused on the pressure C_d because it exhibited a greater difference between the stationary and moving cases. The moving case provided a reduction in the pressure C_d of 11.1% in the middle car and 5.8% growth in the tail car. It was reasonable to attri-

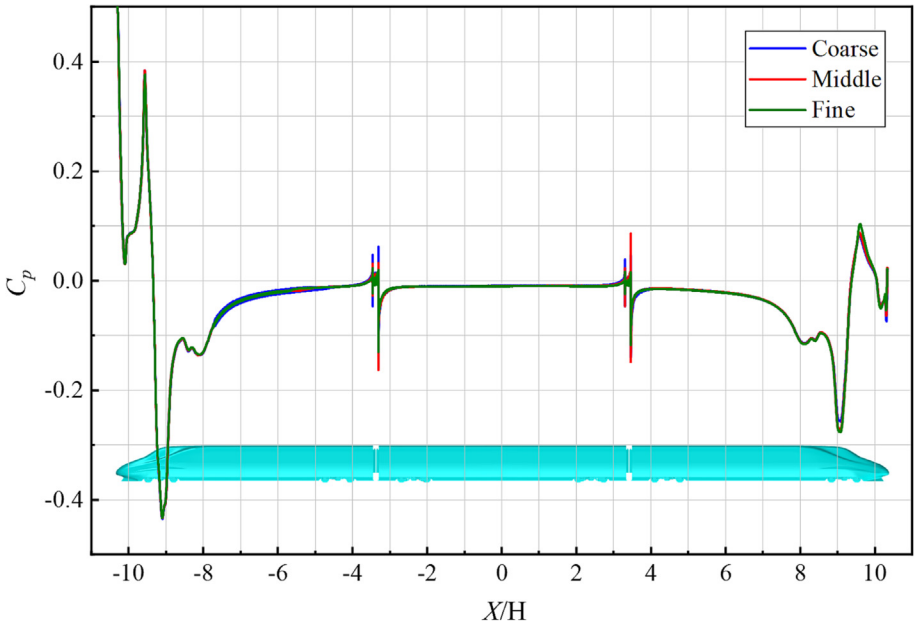

Fig. 6 Comparison of the pressure coefficients for three grids.

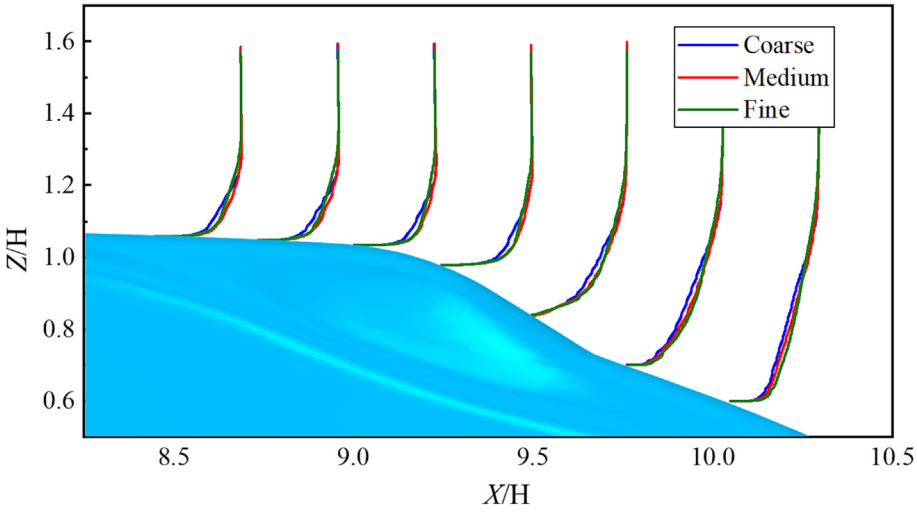

Fig. 7 Time-averaged streamwise velocity at the streamline zone of the tail.

Table 5 Time-averaged C_d values in the stationary and moving cases.

Cases	C_d							
	Viscous				Pressure			
	Head car	Middle car	Tail car	Total	Head car	Middle car	Tail car	Total
Stationary Case	0.059	0.047	0.045	0.151	0.120	0.045	0.104	0.269
Moving Case	0.060	0.049	0.047	0.156	0.116	0.040	0.110	0.266
Difference	1.7%	4.3%	4.4%	3.3%	−3.3%	−11.1%	5.8%	−1.1%

bute the change to the separation vortices at the windshield and wake vortices near the tail nose region. Both of these were difficult to predict precisely. However, the pressure C_d of the middle car was small, and it was prone to larger fluctuations. Therefore, it was more valuable to explore the reasons for the large difference in the C_d value of the tail car.

The maximum and standard deviation (STD) values of the C_d are shown in Table 6. The maximum value was not consistent with the time-averaged C_d. The C_d value of the head car predicted by the stationary case was slightly higher than that of the moving case, while the C_d values of the middle and tail cars were considerably lower than those of the moving case. The STD explained this. Compared with the stationary case, the STDs of the middle and tail cars increased by approximately 15.8% and 26.2%, respectively, in the moving case. This revealed that the middle and tail cars had greater fluctuations in the moving case, so the maximum could fluctuate from the time-averaged value by a large margin. The STD of the head car was relatively small and the maximum was relatively close in the two cases, which was beneficial for the accuracy of the calculation. The pressure drag was related to the pressure distribution, which indicated that the pressure distribution of the head car of the moving case was extremely similar to that of the stationary case.

Fig. 8 shows the spectrum analysis results of the pressure C_d of the head car, middle car, and tail car in both the stationary and moving cases. The Power Spectral Density (PSD) estimate was analyzed based on the monitored pressure C_d time history curve with Welch's method. Each segment was windowed with a Hanning window, and the number of overlapping samples was 50% of the window length. The ordinate was normalized according to the maximum, and the unit of the abscissa frequency f was converted into the Strouhal number $St = \frac{fH}{u_\infty}$. The pressure C_d minus the mean value reduced the direct flux in the frequency spectrum to enhance the recognition of the dominant frequency. As shown in Fig. 8, the most dominant frequency of the moving case was approximately St = 0.31, which was higher than that of the stationary case. In the stationary case, the three cars had different most-dominant frequencies. The reason for the above phenomenon was that the motion of the overset region introduced a dominant frequency. This phenomenon was especially obvious in the tail car. When St = 0.306, the amplitude corresponding to the stationary case was very low, while the maximum amplitude was observed in the moving case. This illustrated the fact that there was a component of the moving case that did not exist in the stationary case. For the head car only, there were multiple dominant frequencies for the differential pressure C_d in the moving case, including two Strouhal numbers with amplitudes exceeding 90% and 80%. The pressure C_d of the middle car showed multiple dominant frequencies in the stationary case. The pressure drag was directly related to the pressure on the upstream and downstream sides, and the pressure was greatly affected by the vortices, especially the separated vortices near the windshield. Therefore, this frequency spectrum also reflected a certain difference in the vortex shedding frequency between the stationary and moving cases. In particular, for the middle car in the stationary case, there was no high-power component similar to that of the moving case near the most-dominant frequency St = 0.303. This difference indicated that there was an inconsistent vortex-shedding frequency of the windshields on both sides. Near the most-dominant frequencies St = 0.226 and 0.121 of the head car and tail car in the stationary case, there were also several strong frequency components in the moving case. This suggested that the difference was caused by the impact of the vortex shedding of the windshield on the head and tail cars, while the similarity was due to the same pressure fluctuations at the noses of the head and tail cars.

3.3. Flow structure

The frequency spectrum analysis of the pressure C_d revealed that the vortices in the stationary and moving cases were significantly different, which motivated the analysis of the flow structure vortices discussed in this section. When the HST was running, the shear and separation of the airflow and the wall produced many flow vortices. To quantify the vortices, the vorticity vector was used to measure the rotation intensity of the flow field. The vorticity is expressed by the curl, and the three direction components are

$$\xi_x = \frac{\partial w}{\partial y} - \frac{\partial v}{\partial z}, \xi_y = \frac{\partial u}{\partial z} - \frac{\partial w}{\partial x}, \xi_z = \frac{\partial v}{\partial x} - \frac{\partial u}{\partial y}$$

The curl is written as $\nabla \times U$, where ∇ is the Hamiltonian operator, and U represents the velocity vector, whose components are u, v, and w. The plane was cut in the X-direction on the side of the tail car close to the windshield, as shown in Fig. 10, and it was colored based on the vorticity X component ξ_x to obtain Fig. 9. A positive value indicated that the flow field rotated clockwise, and a negative value indicated that the flow field rotated counterclockwise.

In Fig. 9 (a), the vorticity is marked with 'SV' (stationary case vortices), where SVG is the abbreviation of the stationary case vortex group. There were six main large-scale vortices near the wall of the train, six small-scale vortices in the SVG, and two small-scale vortices between SV1 and SV6. Fig. 9 (b) shows that there were four main large-scale vortices near the wall of the HST and six small-scale vortices in the MVG (moving case vortex group). Based on the overall scale of the streamwise vortices, the spanwise extension of the moving case was more intense, especially in MV2 and MV5, and

Table 6 Maximum and standard deviation (STD) of pressure C_d.

Cases	C_d					
	Maximum			STD		
	Head car	Middle car	Tail car	Head car	Middle car	Tail car
Stationary	0.154	0.077	0.137	0.0098	0.0101	0.0099
Moving	0.147	0.090	0.151	0.0091	0.0117	0.0125
Difference	−4.5%	16.9%	10.2%	−7.1%	15.8%	26.2%

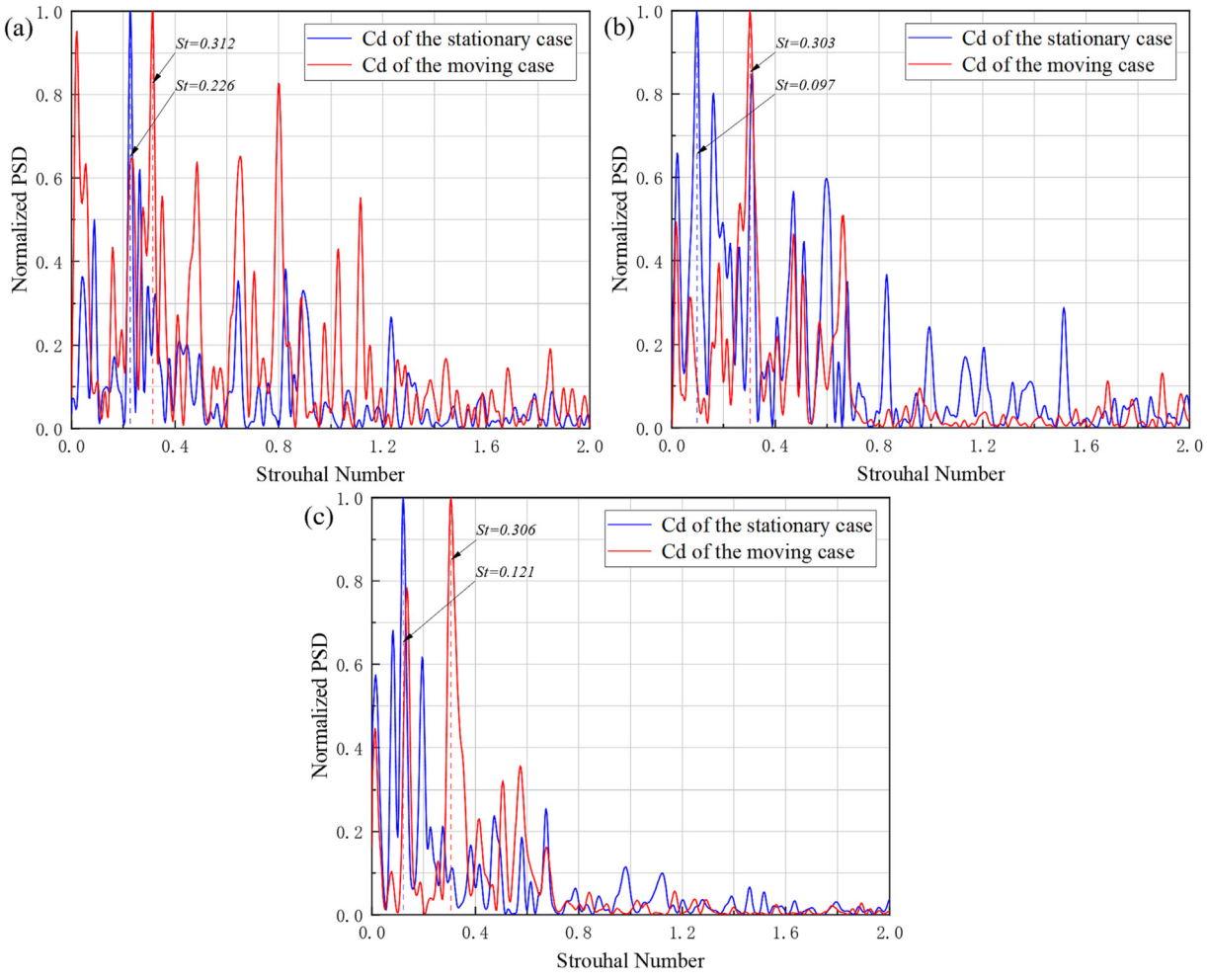

Fig. 8 Comparison of the C_d power spectral density: (a) head car, (b) middle car, and (c) tail car.

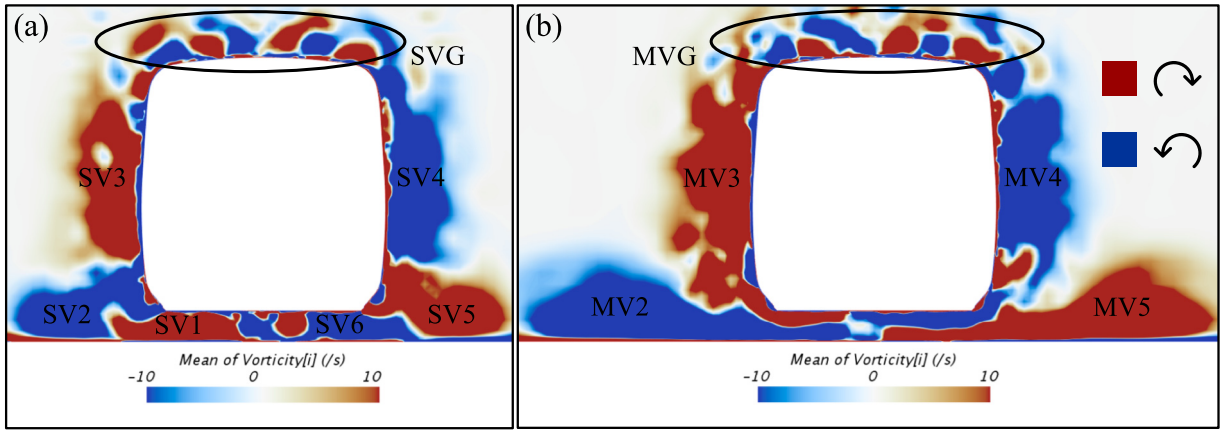

Fig. 9 X-direction vorticity distribution: (a) Stationary case and (b) Moving case.

their vortex cores were significantly far from the HST sidewall. MV3 and MV4 were larger in scale, resulting in a certain expansion in the spanwise direction. The expansion of vortices in the spanwise direction had a significant impact on the rail side pressure fluctuations and slipstream of the HST. The slipstream is described in the following sections.

There were significant differences in the distribution of vortices at the underbody of the vehicle. The tails of MV3 and MV4 and the near-wall sides of MV2 and MV5 in the moving case extended to the underbody of the vehicle to form swirling flow structures arranged vertically. In the stationary case, there were additional vortices SV1 and SV6 at the bottom of the

train, and the two small-scale vortices in opposite directions between them formed a left–right arrangement. The difference in the flow structure at the underbody of the HST directly affected the lift coefficient and the pressure distribution at the bottom of the train.

Compared with the SVG, the vortices showed higher activity in the MVG in the moving case. Its left–right symmetry decreased slightly and there were some broken vortices at the upper half arc of the MVG far from the roof. This suggested that the moving case was more prone to vortex separation and shedding, which might have led to stronger aerodynamic fluctuations in the time domain and enhanced the high-frequency components in the frequency domain.

Although the spanwise and vertical vortex distributions and characteristics were analyzed based on the X-section vorticity figure, the visualization in the streamwise dimension was still lacking in the study of spatial vortex shapes. Fig. 10 shows the distribution characteristics of vortices in the streamwise direction in the stationary and moving cases. The figure mainly contained five elements, including the vector figure, for which only the Y-direction and Z-direction components were used to determine the color. The vortex core in the figure is represented by red tubes, and the surface of the HST and the *iso*-surface for the time-averaged Q-criterion with the value of 16,000 s^{-2} are colored based on the time-averaged pressure coefficient. The plane is colored based on the stream vector. The vector field function used in the vector figure and the vortex core were based on the time-averaged normalized velocity in the stationary case, and the normalized velocity formulas are as follows:

$$U_N = \begin{cases} \frac{u_\infty - u}{u_\infty}(stationary) \\ \frac{u}{u_{train}}(moving) \end{cases}, V_N = \begin{cases} \frac{v}{|u_\infty|}(stationary) \\ \frac{v}{|u_{train}|}(moving) \end{cases},$$

$$W_N = \begin{cases} \frac{w}{|u_\infty|}(stationary) \\ \frac{w}{|u_{train}|}(moving) \end{cases}$$

where U_N, V_N, and W_N represent the normalized velocity components in the streamwise, transverse, and vertical directions. u_∞ represents the incoming flow speed, which was 60 m/s, and u_{train} represents the train's running speed, which was −60 m/s.

To make it easier to compare the stationary and moving cases, the concept of a relative time-averaged normalized velocity was introduced, which was used in the vector diagram and vortex core in the moving case. The formulas are as follows:

$$U_{RN} = \frac{u + u_\infty}{u_\infty}, V_{RN} = \frac{v}{|u_\infty|}, W_{RN} = \frac{w}{|u_\infty|}$$

where U_{RN}, V_{RN}, and W_{RN} represent the relative normalized velocity components in the streamwise, transverse, and vertical directions in the moving case.

Compared with the vorticity figure, the velocity vector figure could more vividly display the location of the vortex core

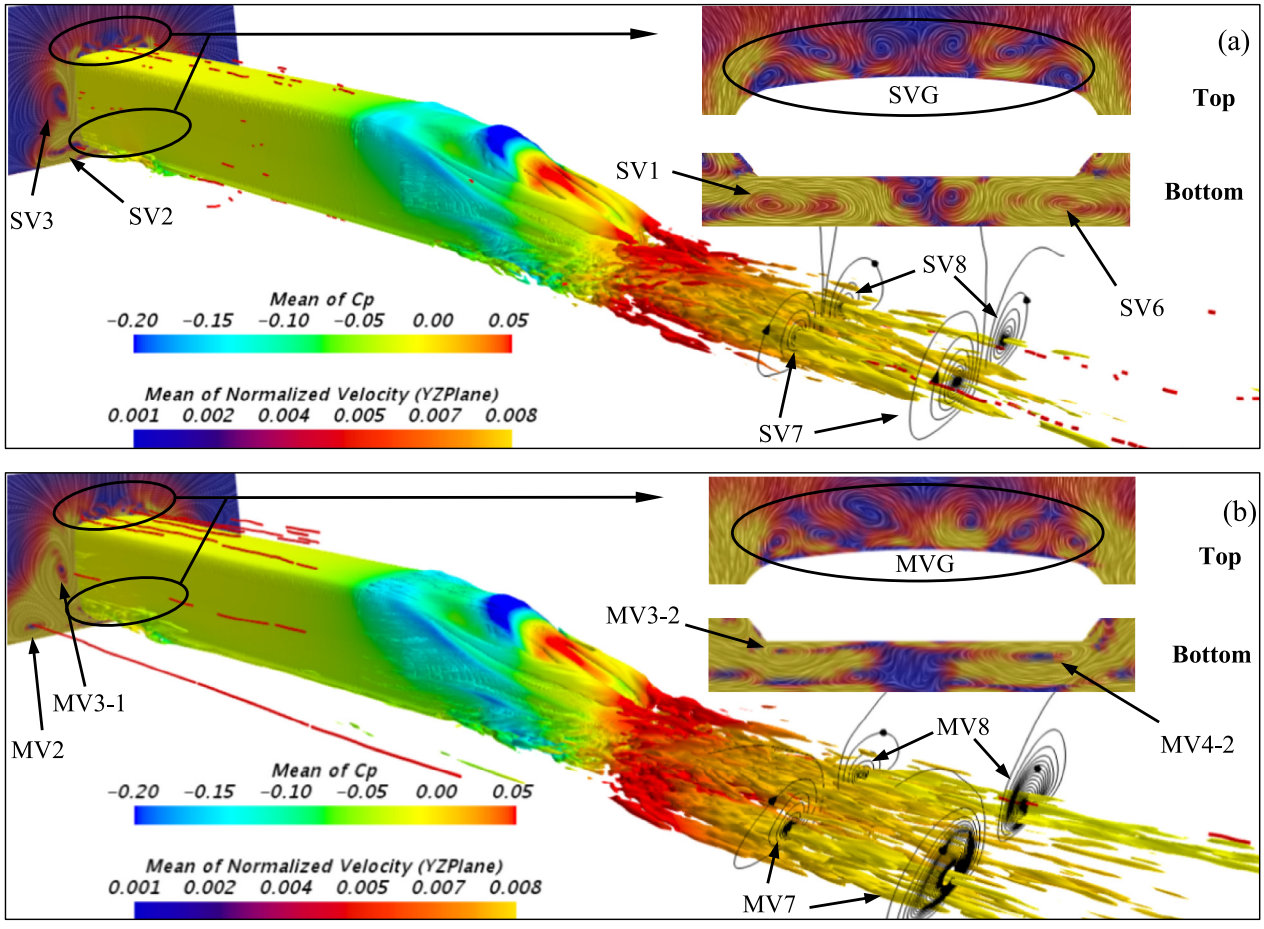

Fig. 10 Distribution of tail car vortices: (a) Stationary case and (b) Moving case.

at the cost of the resolution decreasing. From the enlarged view of the underbody, the vortices in the stationary case were regularly arranged left and right, while those in the moving case were arranged diagonally. Additionally, there was a large low-speed region in the center of the underbody, which significantly changed the pressure. MV3-1 and MV3-2 were two independent vortices with the same rotation direction, which could not be reflected completely in Fig. 9. The same features applied to MV2. In the MVG at the roof of the moving case, the asymmetry of the vortices was more significant.

The evident difference in the vortex cores between the two cases revealed that their vortex distributions along the streamwise direction were very different. The vortex core in the MVG extended significantly along the streamwise direction, and the six vortices had independent and clear vortex cores extending to the position of the streamline zone of the tail car. In the SVG, only the two larger vortices in the middle had strong vortex cores, and the vortex cores of the other four vortices at the edge were not clearly displayed. Similarly, the two large-scale vortices SV2 and SV3 did not have the expected strong vortex cores. In sharp contrast, MV2 and MV3-1, the two large-scale vortices in the moving case, had excellent characteristics in terms of the vortex core length and continuity. The aforementioned results showed that the energy of the streamwise vortex in the stationary case might have been unstable in the streamwise direction, and there were various fluctuations. Because the drawing of the vortex core was based on the (relative) time-averaged normalized velocity, another reason for the difference might have been that the vortex in the stationary case had difficulty maintaining the same vortex structure over the whole sampling time, so there was no clear vortex core, which was the opposite situation to that in the moving case. Although the streamwise vortices of the stationary and moving cases were very different, they still followed the same variation tendency. The vortices in the SVG and MVG only flowed along the streamwise direction, whereas the large-scale vortices on the sides of SV2, SV3, MV2, and MV3-1 flowed along the streamwise direction while gradually moving away from the HST; that is, deviating in the Y-direction.

Although there were vortices with strong energy at the top, underbody, and both sides of the tail car according to the vector figure and vortex core, the isosurface drawn by the time-averaged Q-criterion did not appear. The formula of Q is

$$Q = \frac{1}{2}\left(\|\Omega\|^2 - \|S\|^2\right)$$

where Ω is the spin tensor and S is the strain-rate tensor. When the vortex intensity in the streamwise direction was high, the reason for the low Q value was that the strain rate around the tail car was high, that is, the velocity was too high. This was consistent with the daily observation. It was not easy to observe vortices on either side of the HST. Vortices easily appeared near the wake region of the tail car. Wake vortices are very important structures for an HST that have a direct impact on the aerodynamic performance of the tail car.

The plane streamlines provided an exact indication that the wake vortices were mainly composed of two vortices with opposite rotation directions, named SV7 and SV8 in the stationary case and MV7 and MV8 in the moving case. SV7 and MV7 rotated clockwise and SV8 and MV8 rotated counterclockwise. However, there was a slight difference in the shape of the wake vortices between the stationary case and the moving case. MV7 and MV8 expanded more to the side. In contrast, the shapes of SV7 and SV8 were closer to circles. This was similar to the difference between SV2 and MV2. The isosurface of the wake vortices also reflected the same variation. The span of the isosurface in the Y-direction was small in the stationary case and large in the moving case. In the stationary case, the vortices were concentrated, the vortex core was strong, and the vortices were densely distributed in the downstream region of the wake vortex region, which indicated that the vortices in the stationary case were stable and continuous. In contrast, in the moving case, vortex cores were rare, which might mean that the wake vortex fluctuated and was prone to rupture.

Although the shapes of the wake vortices were different, their formation processes were similar. According to the isosurface, the two air streams entangled with each other after flowing out of the arch and shoulder and finally separated near the tip of the nose. The positions of the two separation points were the same.

3.4. Slipstream

The slipstream was caused by the shear between the HST and the air, which was a characteristic of the HST itself. A slipstream is an important test standard for train operation on an open track because it has a great impact on personnel and basic equipment. The formula for a slipstream is as follows:

$$U_{slip} = \sqrt{U_N^2 + V_N^2}$$

A slipstream has an important impact on the safety of passengers and workers. The Technical Specifications for Interoperability (TSI) has developed detailed monitoring standards. Based on some slipstream conditions described in the TSI, 33 independent and comparable test samples were simulated and sampled in this research, which was higher than the requirement of 20 samples. In the stationary case, the probes were released from the velocity inlet and moved to the pressure outlet at the same speed of 60 m/s as the velocity inlet. The sampling interval of the probe was $\Delta t_{sampling} = 0.25T_{ref}$, and the interval distance between adjacent probes was H. Each probe started 4H upstream of the head car and ended 8H downstream of the tail car.

The slipstreams obtained by each probe are summarized in Fig. 11, and the maximum slipstream values collected by each probe are marked with points. In the vertical axis labels, M represents the moving case, S represents the stationary case, and U represents the platform height, which was 1.4 m from the rail surface (the rail surface was 0.235 m from the ground), and D represents the trackside height, which was 0.2 m from the rail surface. For example, SLU indicates the slipstream at the platform height in the stationary case.

The flow field was divided into three parts: the nose region, the boundary-layer region, and the near-wake region [1]. The nose region extended from upstream of the train to approximately 10 m behind the nose (−14.5H to − 7.5H). The boundary-layer region of the train extended from the end of the nose region to the end of the train (−7.5H to 10.5H). The near-wake region extended approximately 100 m behind the train, where there was a large velocity peak (10.5H–18H).

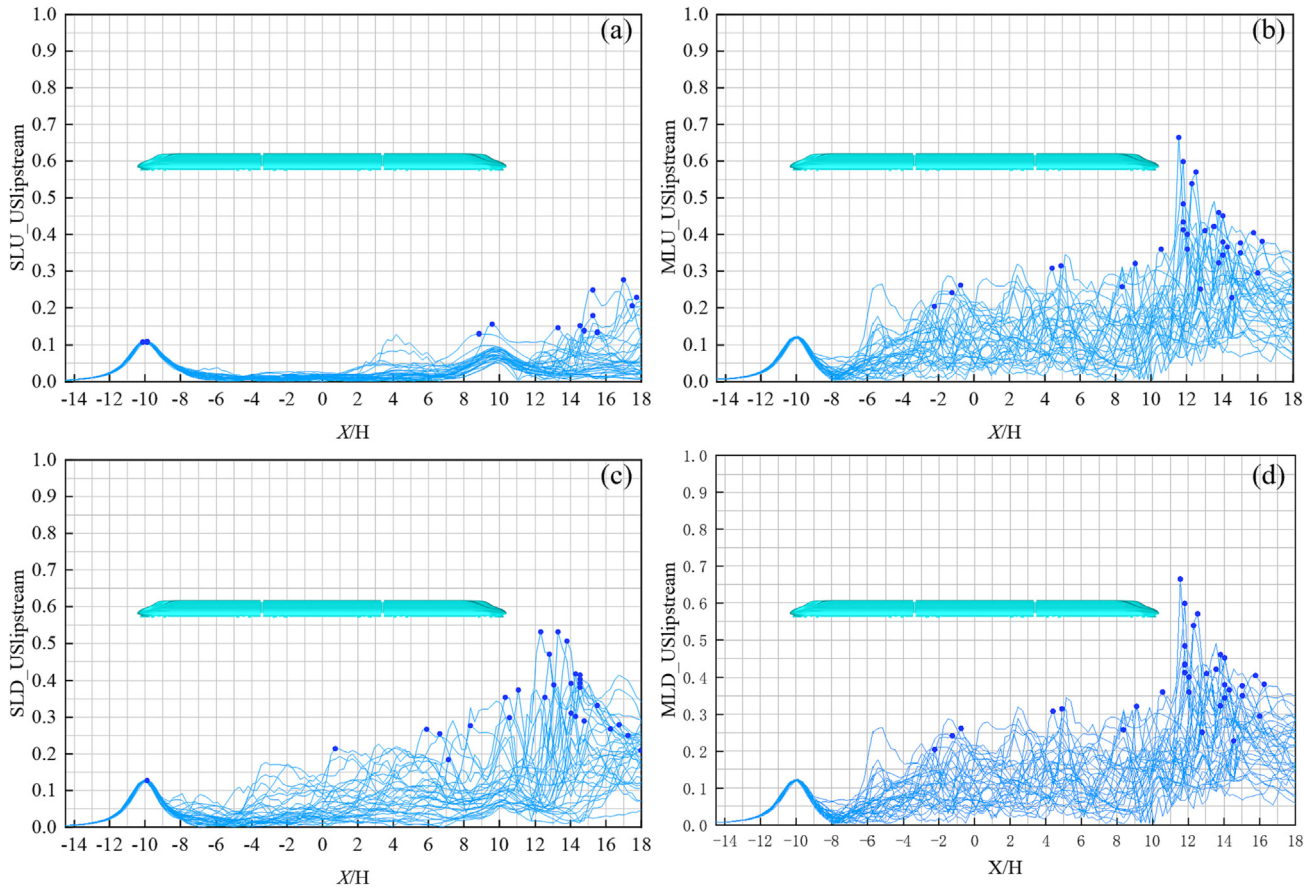

Fig. 11 Thirty-three groups of slipstream measurements: (a) Platform height of the stationary case, (b) Trackside height of the moving case, (c) Trackside height of the stationary case, and (d) Platform height of the moving case.

Each measured data point was independent and had similarities and differences with other data points. All measurements of the slipstream had high coincidence in the nose region and the same peak value, which was the position where the maximum of the partial slipstream occurred. In the boundary layer region, at the platform height, the measurement still maintained partial similarity, the value was small, and few measurement maxima appeared. At the trackside height, the measuring points were deeply affected by vortices MV2 and SV2, the fluctuations of the measured values increased greatly, and some of the maxima of the slipstream appeared. In the near-wake region, the slipstream fluctuated violently, and most of the slipstream maxima appeared in this region because it was controlled by wake vortices. Compared with the stationary case, more maxima of the slipstream in the moving case appeared in the near-wake area, and the values were larger.

The averages and standard deviations of the 33 groups of slipstream data were calculated [39] as shown in Fig. 12. In the nose region, the average slipstream had clear peaks in both the stationary and moving cases, and the difference was small. The peak of the average slipstream at trackside height was slightly greater than that at the platform height, with a difference of 0.015 and a relative difference of 14%. The STDs in the streamline zone of the head vehicle and the zone in front of the nose tip were small, less than 0.01, indicating that the slipstream there was relatively stable in the stationary and moving cases. At the end of the nose region, the STD showed an upward trend.

In the boundary layer region, there were significant differences between the average slipstreams for the moving and stationary cases. The average slipstream at the trackside height in the moving case was approximately 0.045 m/s higher than that in the stationary case, and the average slipstream at the platform height in the moving case was approximately 0.01 m/s higher than that in the stationary case. With the downstream development, the difference between the stationary and moving cases gradually increased, reaching the maximum at the end of the head car and then gradually decreasing. At the end of the boundary layer region, the difference decreased to the minimum. In the process of the slipstream developing downstream, the growth of the average slipstream in the stationary case was relatively stable, while the growth was irregular in the moving case. The STD of the slipstream at the trackside height in the stationary case also increased gradually, indicating that the fluctuation increased gradually. The STD of the slipstream in the moving case fluctuated significantly, and the fluctuation degree was sometimes large and sometimes small. However, the stationary and moving cases had the same variations. At the end of the train position, the slipstream produced a peak that appeared earlier, at approximately 0.7H, at the platform height rather than at the trackside. With the development downstream, the STD of the slipstream gradually increased. The trackside height STD increased from 0.01 to

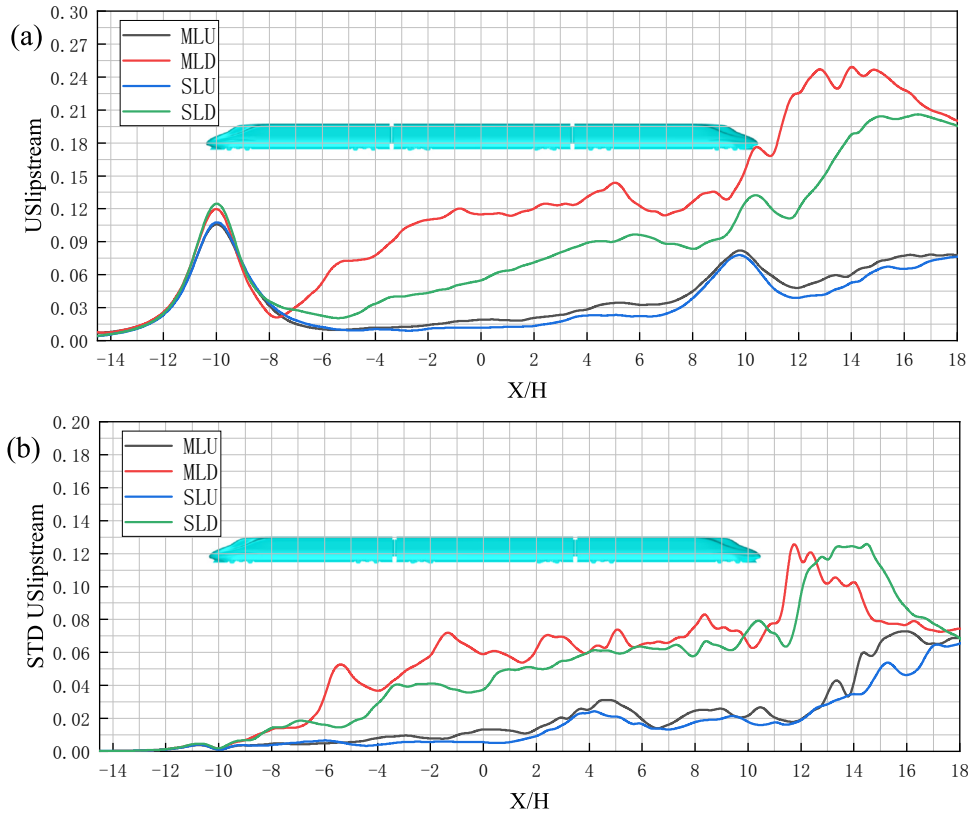

Fig. 12 Average value and standard deviation (STD) of slipstream.

0.06, and the platform height STD increased from 0.005 to 0.02. The STD of the trackside slipstream was significantly greater than that of the platform height slipstream, which indicated that the slipstream at the platform height was relatively stable, while the slipstream at the trackside height fluctuated greatly.

In the near-wake region, the average slipstream first increased and then decreased, and the difference between the average slipstreams of the stationary and moving cases also first increased and then decreased. At the end of the region, the average slipstreams in the stationary and moving cases were almost equal. The STD of the slipstream at the trackside height first increased and then decreased, while the STD of the slipstream at the platform height gradually increased. The two STDs tended to have the same value of 0.07 at the end of the region, and the STDs of the slipstream also tended to have the same value in the stationary and moving cases. This was because the velocity was mainly affected by the wake vortices at 18H, so the STDs at the platform height and trackside height were roughly the same. At the end of the near-wake region, the averages and STDs of the slipstream were the same in the stationary and moving cases. It was concluded that the difference between the two cases ended downstream after a car length, and that the downstream flow fields could be regarded as the same.

Table 7 lists the space-averaged slipstream $\bar{U}_{slip}$, standard deviation σ_{slip}, and $2\sigma_{slip}$ upper limit of the confidence interval $U_{2\sigma}$ at the trackside and platform heights. All of the results in the moving case were greater than those in the stationary case, especially at the trackside height. The main reason for the difference was that the vortex core positions of vortices SV2 or MV2 and SV5 or MV5 were significantly different, resulting in different degrees of influence of the vortices on the probe. The space-averaged slipstreams had a difference of 40%, and the STDs had a difference of 17%. The slipstreams at the platform height were mainly affected by SV3 (or MV3) and SV4 (or MV4) in the stationary case (or moving case). There was little difference between vortices in the previous analysis, so the difference in the space-averaged slipstream at the platform

Table 7 Space-average and STD of the slipstream.

Case	Trackside			Platform		
	$\bar{U}_{\text{slip}}$	σ_{slip}	$\bar{U}_{\text{slip}}+2\sigma_{\text{slip}}$	$\bar{U}_{\text{slip}}$	σ_{slip}	$\bar{U}_{\text{slip}}+2\sigma_{\text{slip}}$
Stationary	0.0869	0.0584	0.2037	0.0355	0.0264	0.0883
Moving	0.1219	0.0685	0.2589	0.0401	0.0266	0.0933

height was much smaller than that at the trackside height, by approximately 13%, and the STD was the same.

4. Conclusion

The goal of this study was to explore the impact of overset mesh motion on the aerodynamic performance of an HST and a flow field structure. There were two scenarios, stationary and moving overset meshes, modeled with the IDDES method. The aerodynamic force, PSD, vortices, and slipstreams were discussed. Based on the numerical predictions, the conclusions were as follows.

(1) With the same spatial and time discretization, when calculating the physical time of the 1/8 high-speed train model for 0.6 s, the calculation core hours required in the moving case were 15% greater than those in the stationary case.
(2) The motion of the overset mesh increased the time-averaged viscous C_d of the train by 3.3% and decreased the time-averaged pressure C_d by 1.1%. The pressure C_d fluctuation intensity of the tail car increased by 26.2% according to STD in the moving case.
(3) While the power spectral density most-dominant frequencies of the pressure C_d of the head car, middle car, and tail car in the stationary case were different, the same most-dominant frequency of St = 0.31 appeared in the moving case. The most-dominant frequencies of the stationary case also existed in the moving case, whose power was slightly lower than the dominant frequency created by the motion.
(4) The motion of the overset mesh expanded the vortices in the spanwise and vertical directions. In the moving case, the vortices were more active and dispersed, including the streamwise vortices around the tail car and the wake vortices. The vortex cores of the streamwise vortices around the vehicle in the moving case were further from the HST.
(5) The motion of the overset mesh increased the average value and standard deviation of the slipstream in the boundary layer region and the upstream area of the near-wake region of the HST. The impact range was approximately from 2H downstream of the head car nose to 8H downstream of the tail car nose.

This research reveals the influence of mesh movement on the calculation results from various angles and provides a reference for the numerical simulation of a train passing through a tunnel or windbreak walls with overset mesh.

Only the motion of overset mesh was studied in this research. There is still a lack of understanding of the numerical simulation errors of sliding and dynamic meshes. Future work will include studying and comparing the main model movement methods, which will help researchers choose the most suitable method for trains when examining the movement mode.

Declaration of Competing Interest

The authors declare that they have no known competing financial interests or personal relationships that could have appeared to influence the work reported in this paper.

Acknowledgments

This work was supported by the Technology Research and Development Program of China Railway (Grant No. Tem. 103), and also in part by the High Performance Computing Center of Central South University.

References

[1] C. Baker, A review of train aerodynamics Part 1 – Fundamentals 118 (2014) 201–228.
[2] M. Gallagher, J. Morden, C. Baker, D. Soper, A. Quinn, H. Hemida, M. Sterling, Trains in crosswinds – Comparison of full-scale on-train measurements, physical model tests and CFD calculations, J. Wind Eng. Ind. Aerodyn. 175 (2018) 428–444, https://doi.org/10.1016/j.jweia.2018.03.002.
[3] J. Tschepe, C.N. Nayeri, C.O. Paschereit, On the influence of Reynolds number and ground conditions on the scaling of the aerodynamic drag of trains, J. Wind Eng. Ind. Aerodyn. 213 (2021), https://doi.org/10.1016/j.jweia.2021.104594 104594.
[4] S. Wang, D. Burton, A.H. Herbst, J. Sheridan, M.C. Thompson, The effect of the ground condition on high-speed train slipstream, J. Wind Eng. Ind. Aerodyn. 172 (2018) 230–243, https://doi.org/10.1016/j.jweia.2017.11.009.
[5] J. Zhang, J. Li, H. Tian, G. Gao, J. Sheridan, Impact of ground and wheel boundary conditions on numerical simulation of the high-speed train aerodynamic performance, J. Fluids Struct. 61 (2016) 249–261, https://doi.org/10.1016/j.jfluidstructs.2015.10.006.
[6] Francesco, Rail Vehicles in Crosswinds: Analysis of Steady and Unsteady Aerodynamic Effects Through Static and Moving Model Tests, 2013.
[7] D. Soper, D. Flynn, C. Baker, A. Jackson, H. Hemida, A comparative study of methods to simulate aerodynamic flow beneath a high-speed train, Proc. Instit. Mech. Eng., Part F: J. Rail Rapid Transit 232 (2018) 1464–1482, https://doi.org/10.1177/0954409717734090.
[8] J. Wang, G. Minelli, T. Dong, K. He, G. Gao, S. Krajnović, An IDDES investigation of Jacobs bogie effects on the slipstream and wake flow of a high-speed train, J. Wind Eng. Ind. Aerodyn. 202 (2020), https://doi.org/10.1016/j.jweia.2020.104233 104233.
[9] E. Deng, W. Yang, X. He, Z. Zhu, H. Wang, Y. Wang, A. Wang, L. Zhou, Aerodynamic response of high-speed trains under crosswind in a bridge-tunnel section with or without a wind barrier, J. Wind Eng. Ind. Aerodyn. 210 (2021), https://doi.org/10.1016/j.jweia.2020.104502 104502.
[10] Z. Guo, T. Liu, Z. Chen, Z. Liu, A. Monzer, J. Sheridan, Study of the flow around railway embankment of different heights with and without trains, J. Wind Eng. Ind. Aerodyn. 202 (2020), https://doi.org/10.1016/j.jweia.2020.104203 104203.
[11] Z. Chen, T. Liu, W. Li, Z. Guo, Y. Xia, Aerodynamic performance and dynamic behaviors of a train passing through an elongated hillock region beside a windbreak under crosswinds and corresponding flow mitigation measures, J. Wind Eng. Ind. Aerodyn. 208 (2021), https://doi.org/10.1016/j.jweia.2020.104434 104434.
[12] F. Dorigatti, M. Sterling, C.J. Baker, A.D. Quinn, Crosswind effects on the stability of a model passenger train—A comparison of static and moving experiments, J. Wind Eng. Ind. Aerodyn. 138 (2015) 36–51, https://doi.org/10.1016/j.jweia.2014.11.009.
[13] A. Premoli, D. Rocchi, P. Schito, G. Tomasini, Comparison between steady and moving railway vehicles subjected to crosswind by CFD analysis, J. Wind Eng. Ind. Aerodyn. 156 (2016) 29–40, https://doi.org/10.1016/j.jweia.2016.07.006.

[14] J. Niu, D. Zhou, Y. Wang, Numerical comparison of aerodynamic performance of stationary and moving trains with or without windbreak wall under crosswind, J. Wind Eng. Ind. Aerodyn. 182 (2018) 1–15, https://doi.org/10.1016/j.jweia.2018.09.011.
[15] Z. Chen, T. Liu, X. Zhou, J. Niu, Impact of ambient wind on aerodynamic performance when two trains intersect inside a tunnel, J. Wind Eng. Ind. Aerodyn. 169 (2017) 139–155, https://doi.org/10.1016/j.jweia.2017.07.018.
[16] X.-F. Liang, X.-B. Li, G. Chen, B. Sun, Z. Wang, X.-H. Xiong, J. Yin, M.-Z. Tang, X.-L. Li, S. Krajnović, On the aerodynamic loads when a high speed train passes under an overhead bridge, J. Wind Eng. Ind. Aerodyn. 202 (2020), https://doi.org/10.1016/j.jweia.2020.104208 104208.
[17] S. Meng, S. Meng, F. Wu, X. Li, D. Zhou, Comparative analysis of the slipstream of different nose lengths on two trains passing each other, J. Wind Eng. Ind. Aerodyn. 208 (2021), https://doi.org/10.1016/j.jweia.2020.104457 104457.
[18] S. Meng, X. Li, G. Chen, D. Zhou, Z. Chen, S. Krajnovic, Numerical simulation of slipstreams and wake flows of trains with different nose lengths passing through a tunnel, Tunn. Undergr. Space Technol. 108 (2021), https://doi.org/10.1016/j.tust.2020.103701 103701.
[19] M. Wang, Y. Mei, Jia Yongxing, Simulation of aerodynamic effects generated by a high-speed train passing through a tunnel with overset grid method, Chinese J. Appl. Mech. 34 (2017) 589-595+618.
65w?>[20] Siemens, STAR-CCM+ User Guide. Version 13.02. (2018).
[21] L. Zhang, M. Yang, X.-F. Liang, Experimental study on the effect of wind angles on pressure distribution of train streamlined zone and train aerodynamic forces, J. Wind Eng. Ind. Aerodyn. 174 (2018) 330–343, https://doi.org/10.1016/j.jweia.2018.01.024.
[22] Z. Zhang, D. Zhou, Wind tunnel experiment on aerodynamic characteristic of streamline head of high speed train with different head shapes, J. Central South Univ. (Sci. Technol.) 44 (2013) 2603–2608.
[23] CEN, Railway applications — Aerodynamics Part 4: Requirements and test procedures for aerodynamics on open track (2013). https://doi.org/10.3403/02796008U.
[24] T. Dong, G. Minelli, J. Wang, X. Liang, S. Krajnović, The effect of ground clearance on the aerodynamics of a generic high-speed train, J. Fluids Struct. 95 (2020), https://doi.org/10.1016/j.jfluidstructs.2020.102990 102990.
[25] X.-B. Li, X.-F. Liang, Z. Wang, X.-H. Xiong, G. Chen, Y.-Z. Yu, C.-M. Chen, On the correlation between aerodynamic drag and wake flow for a generic high-speed train, J. Wind Eng. Ind. Aerodyn. 215 (2021), https://doi.org/10.1016/j.jweia.2021.104698 104698.
[26] CEN, Railway applications — Aerodynamics Part 6: Requirements and test procedures for cross wind assessment (2010). https://doi.org/10.3403/02796008U.
[27] W. Liu, D. Guo, Z. Zhang, G. Yang, Study of Dynamic Characteristics in Wake Flow of High-speed Train Based on POD, J. China Railway Soc. 42 (2020) 49–57.
[28] S. Wang, D. Burton, A. Herbst, J. Sheridan, M.C. Thompson, The effect of bogies on high-speed train slipstream and wake, J. Fluids Struct. 83 (2018) 471–489, https://doi.org/10.1016/j.jfluidstructs.2018.03.013.
[29] J.R. Bell, D. Burton, M.C. Thompson, A.H. Herbst, J. Sheridan, Flow topology and unsteady features of the wake of a generic high-speed train, J. Fluids Struct. 61 (2016) 168–183, https://doi.org/10.1016/j.jfluidstructs.2015.11.009.
[30] S. Wang, J.R. Bell, D. Burton, A.H. Herbst, J. Sheridan, M.C. Thompson, The performance of different turbulence models (URANS, SAS and DES) for predicting high-speed train slipstream, J. Wind Eng. Ind. Aerodyn. 165 (2017) 46–57, https://doi.org/10.1016/j.jweia.2017.03.001.
[31] L. Davidson, Large Eddy Simulations: How to evaluate resolution, Int. J. Heat Fluid Flow 30 (2009) 1016–1025, https://doi.org/10.1016/j.ijheatfluidflow.2009.06.006.
[32] S.B. Pope, Ten questions concerning the large-eddy simulation of turbulent flows, New J. Phys. 6 (2004) 35, https://doi.org/10.1088/1367-2630/6/1/035.
[33] D. Flynn, H. Hemida, D. Soper, C. Baker, Detached-eddy simulation of the slipstream of an operational freight train, J. Wind Eng. Ind. Aerodyn. 132 (2014) 1–12, https://doi.org/10.1016/j.jweia.2014.06.016.
[34] T. Krappel, H. Kuhlmann, O. Kirschner, A. Ruprecht, S. Riedelbauch, Validation of an IDDES-type turbulence model and application to a Francis pump turbine flow simulation in comparison with experimental results, Int. J. Heat Fluid Flow 55 (2015) 167–179, https://doi.org/10.1016/j.ijheatfluidflow.2015.07.019.
[35] P.R. Spalart, S. Deck, M.L. Shur, K.D. Squires, M.K. Strelets, A. Travin, A New Version of Detached-eddy Simulation, Resistant to Ambiguous Grid Densities, Theoret. Comput. Fluid Dyn. 20 (2006) 181–195, https://doi.org/10.1007/s00162-006-0015-0.
[36] M.L. Shur, P.R. Spalart, M.K. Strelets, A.K. Travin, A hybrid RANS-LES approach with delayed-DES and wall-modelled LES capabilities, Int. J. Heat Fluid Flow 29 (2008) 1638–1649, https://doi.org/10.1016/j.ijheatfluidflow.2008.07.001.
[37] X.-B. Li, G. Chen, Z. Wang, X.-H. Xiong, X.-F. Liang, J. Yin, Dynamic analysis of the flow fields around single- and double-unit trains, J. Wind Eng. Ind. Aerodyn. 188 (2019) 136–150, https://doi.org/10.1016/j.jweia.2019.02.015.
[38] G. Gao, F. Li, K. He, J. Wang, J. Zhang, X. Miao, Investigation of bogie positions on the aerodynamic drag and near wake structure of a high-speed train, J. Wind Eng. Ind. Aerodyn. 185 (2019) 41–53, https://doi.org/10.1016/j.jweia.2018.10.012.
[39] The European Commission, concerning a technical specification for interoperability relating to the 'rolling stock — locomotives and passenger rolling stock' subsystem of the rail system in the European Union.